Dynamics of the Mitochondrial Reticulum in Live Cells using Fourier Imaging Correlation Spectroscopy and Digital Video Microscopy

Daciana Margineantu,* Roderick A. Capaldi,* and Andrew H. Marcus†
*Department of Biology and Institute of Molecular Biology, and †Department of Chemistry and Materials Science Institute, University of Oregon, Eugene, Oregon 97403 USA

ABSTRACT We report detailed studies of the dynamics of the mitochondrial reticulum in live cells using two independent experimental techniques: Fourier imaging correlation spectroscopy and digital video fluorescence microscopy. When both methods are used to study the same system, it is possible to directly compare measurements of preaveraged statistical dynamical quantities with their microscopic counterparts. This approach allows the underlying mechanism of the observed rates to be determined. Our results indicate that the dynamics of the reticulum structure is composed of two independent contributions, each important on very different time and length scales. During short time intervals (1–15 sec), local regions of the reticulum primarily undergo constrained thermally activated motion. During long time intervals (>15 sec), local regions of the reticulum undergo long-range "jump" motions that are associated with the action of cytoskeletal filaments. Although the frequency of the jumps depend on the physiological state of the cells, the average jump distance (~0.8 μm) is unaffected by metabolic activity. During short time intervals, the dynamics appear to be spatially heterogeneous, whereas the cumulative effect of the infrequent jumps leads to the appearance of diffusive motion in the limit of long time intervals.

INTRODUCTION

Understanding the relationship between the dynamics of intracellular processes and their biological function is a problem of emerging fundamental importance in cell biology and biophysics. The processes that occur in living cells are complex because they involve interrelated motion of myriad intracellular species on a broad range of spatial and temporal scales. On the scale of small biological molecules (the scale of nanometers), substrates and second messengers diffuse from one enzymatic site to another. On the scale of large molecules (~10–30 nm), protein complexes are assembled and disassembled. Examples are the formation (and destruction) of replication complexes in the nucleus, of translation complexes in the cytosol, and of the permeability transition pore complex in mitochondria. Another important class of cell dynamics involves motion on the scale of the cellular and subcellular levels (0.1–10 μm); organelles may move in response to the timing of the cell cycle or to changes in metabolic conditions. A complete understanding of this complex picture in terms of biological function ultimately requires a detailed understanding of the dynamics of the processes involved.

Because the volumes associated with the intracellular compartment are extremely small, experimental methods for characterizing the movements of intracellular species must use a high degree of signal sensitivity. Traditionally, the most powerful tools are based on measurements of fluorescently labeled specimens due to the inherent sensitivity associated with the detection of optical signals emitted against a dark background. In recent years, fluorescence methods have undergone resurgence as a consequence of technological innovations in optical imaging and detection hardware. State-of-the-art detection equipment is capable of monitoring ultra-low fluorescence signals, in some cases from single isolated molecules (Xie and Trautman, 1998).

Digital video fluorescence microscopy (DVFM) (Saxton and Jacobson, 1997; Marcus, et al., 1996), fluorescence recovery after photobleaching (FRAP) (Chazotte and Hackenbrock, 1991; Partikian et al., 1998; Davoust et al., 1982), and fluorescence correlation spectroscopy (FCS) (Thompson, 1991; Keitling et al., 1998) are three well-established methods that have been successfully used to study intracellular motion. When applied individually, each method has both advantages and disadvantages. DVFM is a means to obtain detailed microscopic dynamical information. However, beyond qualitative interpretations, the meaning of DVFM measurements requires extensive image and computational analysis. Interpretation of FRAP and FCS experiments is more straightforward; collective or self-diffusion coefficients are measured directly, although their values are based on highly model-dependent analyses. Because FRAP and FCS measure ensemble average quantities, it is often difficult to interpret their meaning in terms of the underlying microscopic dynamics that give rise to them.

Here we introduce a new form of correlation spectroscopy, Fourier imaging correlation spectroscopy (FICS), which does not require a model-dependent analysis to extract dynamical information and is designed to fully characterize the dynamics of complex-fluid systems. We apply FICS together with DVFM to study the behavior of a structurally complex intracellular organelle: the mitochondrion.

Recent studies using fluorescence imaging have supported previous electron microscopy work in showing that the mitochondrial fraction of the cell can exist as a single

Received for publication 19 January 2000 and in final form 20 June 2000.
Address reprint requests to Andrew H. Marcus, University of Oregon, Department of Chemistry, Eugene, OR 97403. Tel.: 541-346-4809; Fax: 541-346-4643; E-mail: ahmarcus@fafnir.uoregon.edu.

0006-3495/00/10/1833/17 $2.00

interconnected tubular network, or reticulum (Bereiter-Hahn and Voth, 1994; Rizzuto et al., 1999). Typically, a reticulate mitochondrion extends throughout the cellular interior, filling approximately 20% of the cell volume. The tube-like filaments (~0.5 μm diameter cross-section) are plastic and constantly undergo changes in shape. The details of these motions and their physiological significance are poorly understood, although important functions of the organelle's plasticity have been speculated upon (Bereiter-Hahn and Voth, 1994; Rizzuto et al., 1998). Until now, detailed measurements of these dynamics have not been carried out.

In our FICS measurements, intracellular motion, such as that observed in a fluorescently labeled mitochondrial reticulum, can be detected through time-dependent fluctuations on an experimentally determined length scale, d_G, corresponding to an interference fringe pattern created by two intersecting laser beams. By changing the intersection angle of the laser beams, the wavelength of the detected fluctuations can be varied. The advantage of the FICS method over conventional FCS is that movements can be systematically studied as a function of spatial scale. In this way, it is possible to distinguish normal Fickian diffusion from anomalous diffusion, confined motion, or directed motion, all of which are believed to be important modes of intracellular transport (Saxton and Jacobson, 1997; Luby-Phelps, 1994; Madden and Herzfeld, 1993; Han and Herzfeld, 1993). The FICS measurements directly probe mitochondrial fluctuations over a wide dynamic range (~10^{-4}–10^{2} sec). These measurements yield the time- and wave number-dependent diffusion coefficient and mean-square displacement through analysis of the dynamic structure function. The DVFM measurements generate mitochondrial filament trajectories. We show that Fourier analysis of the trajectories can be used to reconstruct the dynamic structure function, which is found to be in quantitative agreement with the measurements performed using FICS. By using both methods to study the same system, we directly compare statistically averaged dynamical quantities with their microscopic counterparts. Thus, we obtain a microscopic interpretation of the observed rates. The two methods used in combination are a powerful tool to study the dynamics of a complex intracellular organelle such as the mitochondrion.

METHODS

Osteosarcoma cells (143B) were grown in 5-mm-diameter wells created by attaching a perforated layer of sylgard polymer to a glass coverslip. The cells were cultured using HG-DMEM medium supplemented with 10% fetal calf serum, and incubated in 5% CO_2 atmosphere until they reached a 60–80% confluency. For each measurement, the cells were stained for 20 min with 0.25 μM MitoTracker Orange or 0.25 μM JC-1 (Molecular Probes, Eugene, OR). Immediately before data acquisition, another coverslip was placed on top of the sylgard polymer to make a perforated sample chamber. This chamber was sufficient for maintaining the cells in good condition over the duration of a typical measurement (~45 min). For both DVFM and FICS measurements the temperature was maintained at 37 $\pm$ 0.5°C using a water-circulating heating stage equipped with active feedback.

Fourier imaging correlation spectroscopy

The FICS method is described in detail by Knowles et al. (2000). FICS is a new technique that we recently implemented to measure the dynamics of fluorescently labeled complex fluids over a wide dynamic range (~10^{-4}–10^{2} sec) and as a function of spatial scale (~5×10^{-7}–10^{-4} m). Although related methods have been used to study liquid-state dynamics (Hattori et al., 1996; Davoust et al., 1982; Hanson, et al., 1998), this is the first application of a fluorescence experiment that directly measures the time-dependent trajectory of a spatial Fourier component of the fluid density distribution. In our FICS measurements, the experimental observable is the time correlation function (the statistical–mechanical dynamic structure function) that reflects the growth and decay of fluctuations in a spatial Fourier component of the mitochondrial filament areal density profile with wavelength $2\pi k_G^{-1}$. Here k_G ($= 2\pi d_G^{-1}$) is the optically detected wave number. Roughly speaking, the decay time associated with a particular value of k_G is given by $\tau_0 = [D_0 k_G^2]^{-1}$, which is the time required for an unhindered fluorescently labeled filament to diffuse (with diffusion coefficient D_0) the distance k_G^{-1}. The range of k_G probed is significant when compared to key structural features of the mitochondrial reticulum. Although the cross-sectional diameter of a typical filament is ~0.5 μm, the average contour length and the average separation between inter-filament connections is on the order of several microns. For the FICS measurements reported in this work, the range of wave numbers probed is $0.5 \leq 2\pi k^{-1} \leq 1.2$ μm. Thus, our measurements probe the microscopic dynamics of local filament regions.

We show in Fig. 1 a schematic of the FICS apparatus that we assembled and have used in this study. The sample chamber is held on the stage of a microscope and placed at the focus of two intersecting laser beams. The excitation source is the continuous wave frequency doubled output of a Spectra Physics Nd:YAG laser (λ_{ex} = 532 nm); its output power (measured just before sample incidence) is typically set to 1 mW. The laser beam is divided into two optical paths by a Fresnel-rhomb prism and polarizing beam splitter. The transmitted S-polarization component of the beam is rotated 90° using a periscope to match the P-polarization of the reflected beam. The transmitted beam is further passed through an electro-optic phase modulator (Conoptics, Danbury, CT), and then focused onto the sample using a long focal length lens (f = 40 cm). The second beam is reflected by a corner cube mirror mounted on a translation stage before being directed through an identical lens onto the sample chamber. The two beams produce an intensity interference fringe pattern, with adjustable spatial period d_G, inside the sample. The fringe spacing depends on the intersection angle, θ, between the two beams (Fleming, 1986):

$$d_G = \frac{\lambda_{ex}}{2 \sin(\theta/2)}. \quad (1)$$

The fringe spacing, d_G, can be adjusted continuously between tens of microns (for the case of small θ) and $\lambda_{ex}/2$ (for the case of counter propagating beams).

The fluorescence emitted from the overlap of the labeled filaments and the oscillatory excitation fringe pattern is imaged onto a detector using a fused silica objective lens (Plan Fluotar, 100×, N.A. = 1.3, oil immersion, Leica, Deerfield, IL) and eyepiece (5×, Zeiss, Thornwood, NY). The image depth-of-field is limited by placing an adjustable aperture (~50 μm) at the focal plane conjugate to the sample. For the FICS measurements, the emission is coupled into a multimode optical fiber (3M). The emission from the transmitting end of the fiber is imaged onto a thermoelectrically cooled photomultiplier tube (R3896, Hamamatsu, Bridgewater, NJ) after filtration by an interference filter (central wavelength 590 nm, bandwidth

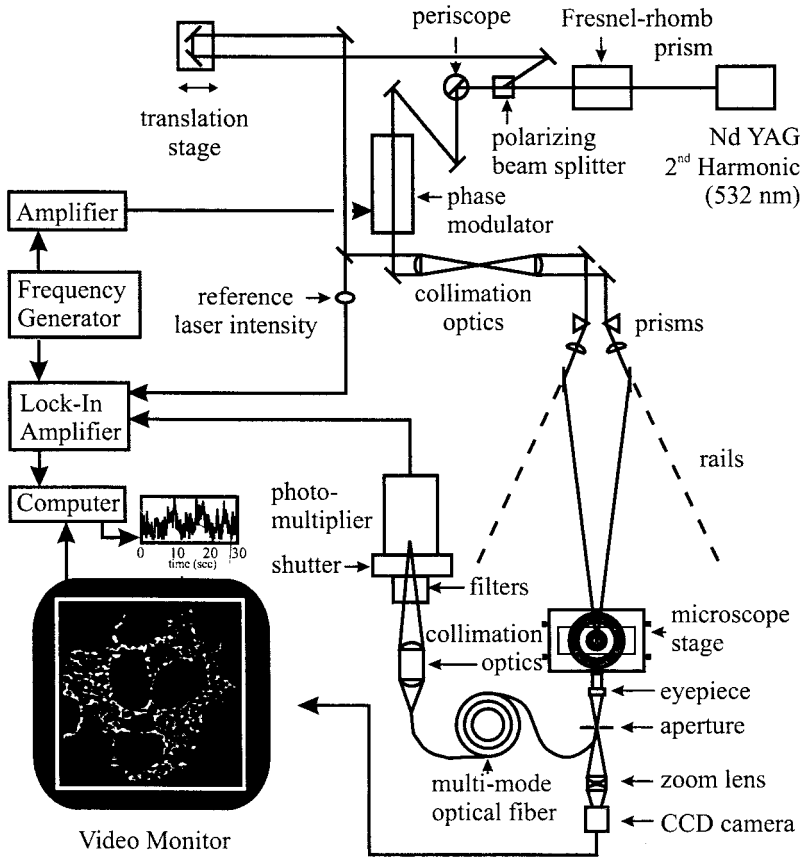

FIGURE 1 Schematic illustration of the FICS apparatus used in the reported studies.

10 nm, transmission efficiency 90%, CVI Laser, Livermore, CA) and an excitation barrier filter (532 nm). At any instant in time, the oscillatory excitation profile picks out a small set of spatial Fourier components of the labeled particle distribution. There is a primary component at wavenumber $k_G = |\mathbf{k}_G| = 2\pi d_G^{-1}$, in addition to a $|\mathbf{k}| = 0$ component associated with the mean fluorescent light level, and a band of small-k contributions associated with the Gaussian envelope of the illuminated region. Temporal fluctuations in the integrated fluorescence intensity, $\delta I(t) = I(t) - \langle I \rangle$, reflect the growth and decay of the spatial Fourier components represented by the image. Slow fluctuations of the chromophore distribution associated with the small-k spatial components arise from filaments moving in and out of the illuminated Gaussian envelope and from slow drifts in the alignment of the laser spots. Other components of the signal include low-frequency mechanical vibrations and $1/f$ shot-noise in the detection electronics.

Fluctuations of the signal due solely to number density fluctuations at wavenumber k_G are selectively measured using the method of lock-in detection. A frequency generator (Keithley) is used to send an amplified saw-tooth waveform to the phase modulator to drive the relative phases of the two beams from 0 to 2π at a frequency, ω_G, of 10 kHz. The excitation fringe pattern is thus swept across the illuminated sample region at a velocity, v_G ($=\omega_G/k_G$), greater than that with which a filament can travel the distance $2\pi k_G^{-1}$. The modulated signal output of the photomultiplier tube is detected using a lock-in amplifier (Stanford Research Systems) that is referenced to the signal waveform used to drive the phase modulator. A personal computer records separately (1) the average background fluorescence intensity, $\kappa I_0 \hat{C}(0)$ (DC signal component, defined below), (2) the instantaneous fluorescence modulation amplitude, $A(t) = \kappa I_0 |\hat{C}(k_G, t)|$ (AC signal component, defined below), which arises due to the sweeping of the fringe pattern and whose magnitude varies as a result of filament fluctuations at $k = k_G$, and (3) the laser excitation power. All contributions to the noise that are not correlated with the modulation frequency (including filament fluctuations corresponding to $k \neq k_G$) are suppressed.

FICS was used to study the dynamics of mitochondria in cells stained with JC-1 and MitoTracker Orange. Multiple experiments were performed at three different fringe spacings (d_G = 0.55, 0.82, and 1.0 μm). For each experiment, 16,000 data points were collected at an acquisition frequency of 8 Hz. Under these conditions, the signal-to-background ratio of the modulated fluorescence amplitude, $\langle \delta A^2 \rangle^{1/2}/\hat{C}(0)$, was found to be ~50%. The extent of photodegradation over the duration of a 30-minute test measurement represented less than 20% loss of the total fluorescence signal. In practice, the total fluorescence intensity, after being corrected for drifts in laser power (less than $\pm$1%), was used to normalize the time-dependent modulation amplitude, effectively removing the influence of photodegradation on the overall fluctuation signal. To determine the effects of laser-induced photodamage on our measurements, we performed a power-dependence study. Laser excitation intensities up to 10 mW resulted in identical autocorrelation functions to those obtained using 1 mW. However, the amount of photodegradation was significantly increased, resulting in a 90% signal loss. Thus, at the relatively low excitation powers used in these studies, photodamage did not affect our measurements of mitochondrial dynamics.

The total instantaneous fluorescence intensity emitted from the excitation grating, $I_G(t)$, is proportional to the spatial overlap of the time-dependent oscillatory excitation profile and the time-dependent distribution of fluorescently labeled filaments, $C(\mathbf{r}, t)$ [see Eq. 9, below] (Knowles et al., 2000). In the limit where the laser beam diameter is much larger than d_G, the excitation profile can be well approximated by an infinite two-dimensional fringe pattern modulated in the direction of the x-axis, and the

signal can be written

$$I_G(t) = \kappa I_0 \int C(\mathbf{r}, t)\{1 + \cos[\mathbf{k}_G \cdot (\mathbf{x} + v_G t)]\}\mathrm{d}^3 r$$
$$= \kappa I_0\{\hat{C}(0) + |\hat{C}(\mathbf{k}_G, t)|\cos[k_G v_G t + \alpha(\mathbf{k}_G, t)]\}, \quad (2)$$

where v_G is the velocity with which the fringe pattern travels across the sample, $\hat{C}(\mathbf{k}_G, t)$ is the spatial Fourier transform of the filament distribution, $C(\mathbf{r}, t)$, evaluated at $k = k_G$ and α is the phase angle associated with $\hat{C}$, namely $\alpha = \tan^{-1}[\mathrm{Im}\,\hat{C}/\mathrm{Re}\,\hat{C}]$. The vectors $\mathbf{k}_G$ and v_G are antiparallel and indicate the propagation direction of the fringe pattern. The constants κ and I_0 represent the luminescence efficiency and incident laser intensity, respectively. Eq. 2 shows that the total signal is composed of a stationary and modulated component. The stationary component, $\kappa I_0 \hat{C}(0)$, corresponds to the mean fluorescence background, whereas the modulated component contains information about the distribution $\hat{C}(\mathbf{k}_G, t)$ through its modulus, $|\hat{C}|$, and phase angle α. The time-dependent fluctuations of $I_G(t)$ $[\delta I_G(t) = I_G(t) - \langle I_G \rangle]$ arise for two reasons. As the fringe pattern is swept across the sample with velocity v_G, the total fluorescence signal is modulated at the angular frequency $k_G v_G$. The modulation amplitude, $A(t) = |\hat{C}|$, depends on the extent to which the heterogeneous spatial distribution of filaments contains some periodicity with wavelength d_G. The velocity v_G is set to an arbitrary value greater than the average velocity of the mitochondrial filaments. As $C(\mathbf{r}, t)$ fluctuates in time due to the "slow" motion of the labeled filaments, its periodicity with wavelength d_G also fluctuates, resulting in slow variation of the modulation amplitude from its average value $[\delta A(t) = A(t) - \langle A \rangle]$. The time-dependence of $\delta A(t)$ contains the k-dependent dynamical information we wish to study.

Using a diffusion equation of motion, we obtain the normalized autocorrelation function of $\delta I_G(t)$ (Hattori et al., 1996),

$$\frac{\langle \delta I_G(t)\delta I_G(t+\tau)\rangle}{\langle \delta I_G(t)^2\rangle} = \left[\left(1 + \frac{4D_b\tau}{b^2}\right)^{-1} + \tfrac{1}{2}\cos(k_G v_G \tau)\cdot\exp(-k_G^2 D_{\mathrm{eff}}\tau)\right]. \quad (3)$$

The first term in Eq. 3 represents the background motion of filaments entering or leaving the Gaussian envelope of the two intersecting laser beams, with b ($\cong 100\ \mu$m) the $1/e$ beam radius and D_b the characteristic diffusion coefficient of this process. The second term in Eq. 3, which oscillates at the angular frequency $k_G v_G$, describes the local filament mobility characterized by the so-called "effective" diffusion coefficient, $D_{\mathrm{eff}} = \tilde{D}(k = k_G, \tau)$, observed on the length scale d_G and incremental time τ.

To selectively measure the second term in Eq. 3, we use lock-in amplification. The lock-in amplifier rejects the relatively large DC component of $I_G(t)$ and measures its relatively small instantaneous modulation amplitude, $A(t)$. Because fluctuations in $A(t)$ reflect the motion of the mitochondrial filaments at wave number k_G, we can write the normalized autocorrelation function of $\delta A^2(t)$ (Hattori, 1996)

$$G_k(\tau) = \frac{\langle \delta A^2(t)\delta A^2(t+\tau)\rangle}{\langle \delta A^2(t)\rangle^2} = \exp[-2k_G^2 D_{\mathrm{eff}}\tau]. \quad (4)$$

$G_k(\tau)$ is a wave number-dependent time-correlation function whose decay is characterized by the same effective diffusion coefficient that appears in the second term of Eq. 3. The connection between $G_k(\tau)$ and the microscopic motion of mitochondrial filaments can be understood in terms of liquid state theory (Balucani and Zoppi, 1994). According to Eq. 2, the detected fluorescence signal can be interpreted as an instantaneous Fourier component of the filament distribution,

$$\hat{C}(\mathbf{k}_G, t) = \frac{1}{\sqrt{N}}\sum_j e^{i\mathbf{k}_G\cdot\mathbf{r}_j},$$

at wavevector $\mathbf{k}_G$. The temporal autocorrelation function of $\hat{C}(\mathbf{k}_G, t)$ is proportional to the microscopic dynamic structure of the mitochondrial filaments,

$$F(k,\tau) = \langle \hat{C}^*(\mathbf{k}, t)\hat{C}(\mathbf{k}, t+\tau)\rangle = N^{-1}\sum_i\sum_j \langle \exp\{i\mathbf{k}\cdot[\mathbf{r}_i(t) - \mathbf{r}_j(t+\tau)]\}\rangle, \quad (5)$$

where $k = |\mathbf{k}|$. Because we are interested in high-k measurements applied to semidilute systems of entangled filaments, the cross terms in Eq. 5 do not contribute to their respective sums, leaving only the self terms. Thus, Eq. 5 reduces to (Berne and Pecora, 1976)

$$F_S(k,\tau) = \langle \exp\{i\mathbf{k}\cdot[\mathbf{r}(t) - \mathbf{r}(t+\tau)]\}\rangle, \quad (6)$$

where $F_S(k, \tau)$ is the self-part of the intermediate scattering function.

To relate Eq. 6 to the effective diffusion coefficient, we use the Gaussian model for single particle motion (Berne and Pecora, 1976). The Gaussian model makes use of the fact that the time scale associated with observation of the local filament displacements is large compared to the relaxation time of the velocity autocorrelation function of the local filament positions. In this case, $[\mathbf{r}(t) - \mathbf{r}(t+\tau)]$ may be treated as a Gaussian random variable, which leads Eq. 6 to take the following form for two dimensions,

$$F_S(k,\tau) = \exp\left[-\frac{k^2}{4}\langle[\mathbf{r}(t) - \mathbf{r}(t+\tau)]^2\rangle\right] = \exp[-k^2 W(\tau)] = \exp[-k^2\tilde{D}_S(k,\tau)\tau], \quad (7)$$

where $W(\tau) = \langle[\mathbf{r}(t) - \mathbf{r}(t+\tau)]^2\rangle/4$ is the effective two-dimensional mean square displacement of a local filament region and $\tilde{D}_S(k, \tau) = W(\tau)/\tau$ is the effective self-diffusion coefficient measured at wave number k. Comparison between Eqs. 4 and 7 leads to

$$[G_k(\tau)]^{1/2} = F_S(k,\tau) = \exp[-k^2 W(\tau)] = \exp[-k^2\tilde{D}_S(k,\tau)\cdot\tau]. \quad (8)$$

We conclude that the experimental observable measured in our FICS experiments is directly related to the self-displacements of local mitochondrial filaments as described by Eq. 8.

The similarity between Eqs. 4 and 7 is not coincidental. In each case, the assumption of Fickian dynamics was made. For a system that strictly obeys Fickian dynamics, the effective self-diffusion coefficient is expected to be constant whereas the mean square displacement is a linear increasing function of time. For a system that does not obey Fickian dynamics, the diffusion coefficient is time-dependent. The extent to which $\tilde{D}_S(k, \tau)$ deviates from Fickian behavior is an indication of the system exhibiting, on average, a mode of motion more complex than pure diffusion.

Digital video fluorescence microscopy

DVFM is a powerful technique that has been applied to the study of biological systems (Rizzuto et al., 1998b; Saxton and Jacobson, 1997) and to complex fluids (Crocker and Grier, 1996; Marcus et al., 1996, 1999).

We perform DVFM measurements on mitochondria samples using a Zeiss UEM fluorescence microscope with a 100×, numerical aperture 1.3, oil immersion objective lens (Ultrafluar, Zeiss). The excitation source is a Coherent Nd:YAG laser operating in continuous wave (cw) mode at 532 nm; its output power is typically set to below ~1 mW (as detected at the sample). Samples are exposed to the excitation light by epi-illumination and the fluorescence emission is relayed to the camera eyepiece via a dichroic beamsplitter (550–615-nm transmission). Fluorescence images of the sample are collected using an image intensified charge coupled device (CCD) digital video camera mounted to the camera eyepiece (16 bit, Gen V, Princeton Instruments, Trenton, NJ). The frame speed of the CCD is adjustable; images are acquired at a rate ranging between 0.05 and 1 Hz. Exposure times for each image is typically set within the range 0.8–1.0 sec. During the time intervals between successive frames, a mechanical shutter is used to block the laser excitation such that the total sample exposure time does not exceed 1 sec per captured image. The Princeton Instruments frame grabber supplied with the CCD is used to digitize sequences of 512 × 512 square pixel frames. A typical run consists of 100 frames in sequence, corresponding to roughly 250 Mbytes of data. All image-processing procedures are implemented using IDL (Research Systems, Inc.), a programming language optimized for visual data analysis. The pixel length is calibrated by imaging a transmission electron microscope grid of known scale. The aspect ratio is determined to be 1 ± 0.1 and the calibrated pixel dimension is 1 pixel = 0.178 μm for 100× magnification and 1 pixel = 0.0699 μm for 250× magnification.

Unlike FICS, the observable in a DVFM experiment is a complete set of two-dimensional N filament position trajectories,

$$C(\mathbf{r}, t) = \sum_{i=1}^{N} \delta[\mathbf{r} - \mathbf{r}_i(t)]. \tag{9}$$

Here we designate the filament positions as a locus of points that define the instantaneous configuration of all filaments visible in the image. In DVFM, the minimum sampling time interval is determined by the time step between consecutive configurations. The experimental procedure is to image a representative area of the sample onto the detector face of a high resolution CCD video camera. The video signal is subsequently converted into storable digitized information using a frame grabber. The process of transforming the information contained in a sequence of digitized images into the time-dependent density profile described by Eq. 9 is given by a prescription involving five logical steps. Here we provide a rough outline of the procedure.

1. Image restoration: The raw data images usually contain various defects that hinder immediate analysis. These include long wavelength contrast gradients and random pixel noise. The background artifacts are nominally due to uneven illumination or sensitivity of the camera pixels, whereas pixel noise is associated with the instrument response of the CCD camera and the frame grabber. Because pixel noise is nearly random with a correlation length λ_n equal to one pixel, it is greatly reduced by convolving the raw data image with a Gaussian surface of half-width λ_n. This operation suppresses the noise without noticeably decreasing the contrast. The resulting "noise reduced" image is further enhanced by subtracting off the "background" image. This background is constructed by performing a boxcar average of the raw data with a step size equal to $2w + 1$, where w is the apparent feature radius measured in pixels. The end result is an estimate of an ideal image that can be further processed.
2. Location of filament positions: The filtered images are analyzed to determine the locations of local brightness maxima. A pixel position is designated as a local maximum if only one other pixel within a distance w has a larger value. Typically, the number of candidate local maxima found is larger than the number of filament positions in the frame. Because the maxima corresponding to the filament positions are the brightest of those found, only the brightest 30% of the candidates are accepted.
3. Refining candidate positions: The local maximum algorithm described by steps 1 and 2 is sufficient to resolve filament positions to within half a pixel. The spatial resolution is improved by calculating the brightness-weighted centroid positions from the spatial integral of circular areas with radius w centered at the original uncorrected positions. This correction is smaller than 0.5 pixel and has the overall effect of improving the resolution to 0.1 pixel.
4. Candidate filament position discrimination: In addition to the integrated brightness within a circular area of radius w centered about each candidate position (m_0), the second moment of the brightness distribution (m_2) is also calculated. It is found that filament and nonfilament candidates form two distinct well-separated distributions in the (m_0, m_2) plane. The candidates corresponding to the true filament positions are selected based on this criterion.
5. Linking sequential configurations into filament position trajectories: In this final step, it is necessary to determine which filament positions in a given image correspond to subsequent positions in later images. For dilute suspensions, the mean separation is much larger than single-filament position displacements, which are typically much smaller than the dimensions of a filament diameter. Therefore, all trajectory displacements of interest are easily identified because they fall within an empirically determined cutoff range.

Several properties can be calculated from the trajectory data (Eq. 9) using the methods of statistical mechanics (Marcus, et al., 1996, 1999). Here we focus on the intermediate scattering function to compare with our FICS results. In principle, it is possible to calculate $F_S(k, \tau)$ directly from the trajectory data. This is accomplished in two ways. First, we consider the microscopic definition,

$$F(\mathbf{k}, \tau) = \langle \hat{C}^*(\mathbf{k}, t)\hat{C}(\mathbf{k}, t + \tau)\rangle, \tag{10}$$

where $\hat{C}(\mathbf{k}, t)$ is the Fourier transform of the spatial filament position density Eq. 9 given by

$$\hat{C}(k,t) = \left(\frac{1}{N}\right)^{1/2} \int d\mathbf{r} \exp(-i\mathbf{k}\cdot\mathbf{r})C(\mathbf{r}, t). \tag{11}$$

For nonzero k, the combination of Eqs. 11, 9, and 10 results in an expression for $F(k, \tau)$ that is an explicit function of $\mathbf{r}(t)$ given by the statistical average Eq. 5. This expression is evaluated numerically using standard computer simulation techniques (Allen and Tildesley, 1987). Alternatively, image-processing algorithms are used to calculate $F(k, \tau)$ from "idealized" images constructed from the filament trajectories. These ideal images are numerically Fourier transformed in two dimensions using standard fast Fourier transform algorithms. Eq. 10 is evaluated by calculating the time autocorrelation function of the Fourier space images for a particular time interval, averaged over many filament configurations.

Using these two independent methods of evaluating $F(k, \tau)$ from the microscopic data, we were able to check for self-consistency of the results for a single set of filament trajectories. We also examined the differences between the full intermediate scattering function and the self part, $F_S(k, \tau)$. As discussed above, neglecting the cross terms ($j \neq i$) in Eq. 5 leads to an expression (Eq. 6) for $F_S(k, \tau)$. For the microscopy data presented in this work, the filament concentrations were small enough that the self and full intermediate scattering functions were indistinguishable by the methods described above. Therefore, the previous assertion that these measurements correspond to the microscopic regime was experimentally verified.

RESULTS

In Fig. 2 we show three-dimensional reconstructions of confocal fluorescence micrographs of an osteosarcoma cell

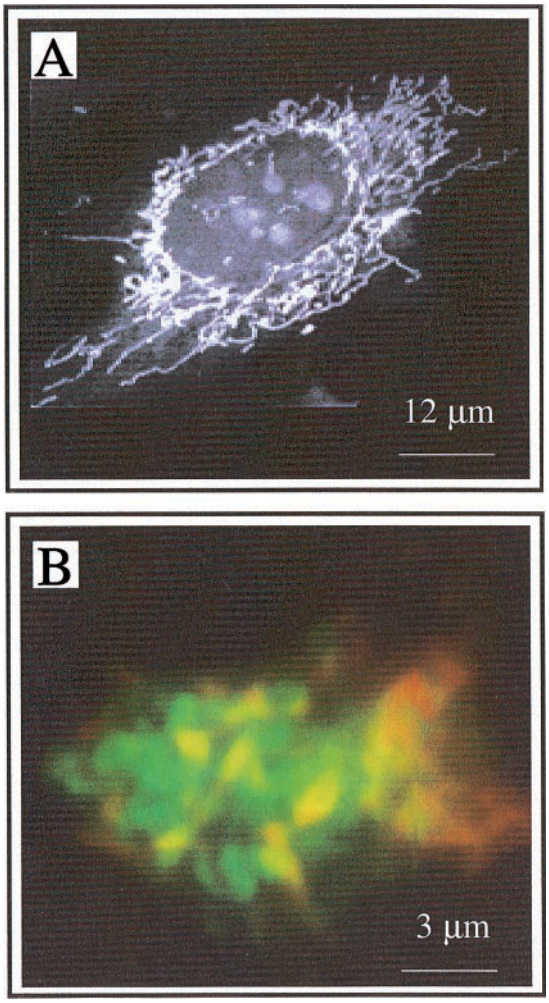

FIGURE 2 (*A*) Three-dimensional reconstruction of a confocal fluorescence image of an osteosarcoma cell labeled with a green fluorescent protein construct targeted to the mitochondrial matrix space. The reticulate structure of the mitochondria is evident. (*B*) High-magnification image of reticulate mitochondrial filaments stained with JC-1 dye.

transfected with green fluorescent protein targeted to the matrix space (Fig. 2 *A*) and a high-power magnification image of mitochondria stained with JC-1 (Fig. 2 *B*). In both images, the mitochondrion of the cell is fluorescently labeled and appears as a single interconnected tubular network of filaments (i.e., a reticulum). Additional work using serial-sectioning techniques and transmission electron microscopy confirms that the mitochondrion exists as a reticulum in these cells (Gilkerson, et al., 2000). JC-1 is a positively charged carbocyanine dye that is known to be a quantitative fluorescence indicator of membrane potential, $\Delta\Psi$ (Reers et al., 1991, 1995; Salvioli et al., 1997). Under favorable physiological conditions and above a critical threshold concentration, JC-1 forms a concentration-dependent fluorescent nematic phase consisting of J-aggregates. When excited at 488 nm, the monomers exhibit an emission maximum at 527 nm (green regions) and J-aggregates at 590 nm (red regions). Increasing JC-1 concentration results in a proportionate rise in J-aggregate fluorescence without affecting monomer fluorescence. The membrane potential of energized mitochondria is polarized such that the matrix space has a net negative charge. Local regions of the membrane that are energized promote an uptake of JC-1 into the matrix with subsequent formation of J-aggregates.

It is evident from Fig. 2 *B* that the spatial distribution of $\Delta\Psi$ in reticulate mitochondria, as visualized by JC-1 monomer/J-aggregate emission, appears heterogeneous under control physiological conditions. This spatial heterogeneity is sensitive to the metabolic state of the cell. In Fig. 3, we show fluorescence micrographs of JC-1-labeled cells after exposure to various drugs (listed in Table 1). Nigericin is an ionophore that exchanges K^+ and H^+ across the mitochondrial inner membrane, resulting in uncoupling of respiration from adenosine triphosphate production. The net effect of Nigericin treatment is the hyperpolarization of the mitochondrial inner membrane. The spatial distribution of $\Delta\Psi$ becomes uniformly large throughout the reticulum after ~30 min incubation with Nigericin (Fig. 3 *B*). Inhibition of respiration can be achieved with Antimycin A, which inhibits the activity of mitochondrial respiratory chain complex III. Cells treated with Antimycin A (~10-min incubation) show a progressive decrease in local membrane regions with high $\Delta\Psi$ (Fig. 3 *C*). Staurosporine is a protein kinase inhibitor that induces apoptosis (programmed cell death). Dramatic changes in mitochondrial membrane morphology are observed in cells that have been treated with Staurosporine (~4-h incubation). This drug has the initial effect of hyperpolarizing the mitochondrial membrane accompanied by membrane swelling, followed by the disruption of mitochondria structure with the formation of megamitochondria and cell blebbing (Fig. 3 *D*).

We studied the motion of hyperpolarized regions of the mitochondrial membrane under various conditions by detecting only those regions of the images that emit at 590 ± 5 nm. Control experiments were also performed on cells treated with MitoTracker Orange (CM-H_2TMRos), a rhodamine-based dye that becomes fluorescent after it is oxidized in actively respiring regions of the mitochondria and irreversibly binds to mitochondrial proteins. MitoTracker Orange is insensitive to transient behavior of $\Delta\Psi$. For cells treated with either JC-1 or MitoTracker Orange, the excitation and detection wavelengths were 532 and 590 nm, respectively.

When these cells are visualized in the fluorescence microscope, movements of the reticulum filaments can be observed. In Fig. 4, we show a single restored image frame taken from a DVFM data set of a cell treated with MitoTracker Orange under control physiological conditions. Also shown are the assignments of local filament positions and the associated trajectories of the full 100-frame sequence (1 frame s^{-1}). The pathways taken by individual filament regions appear to be unbiased by the possible

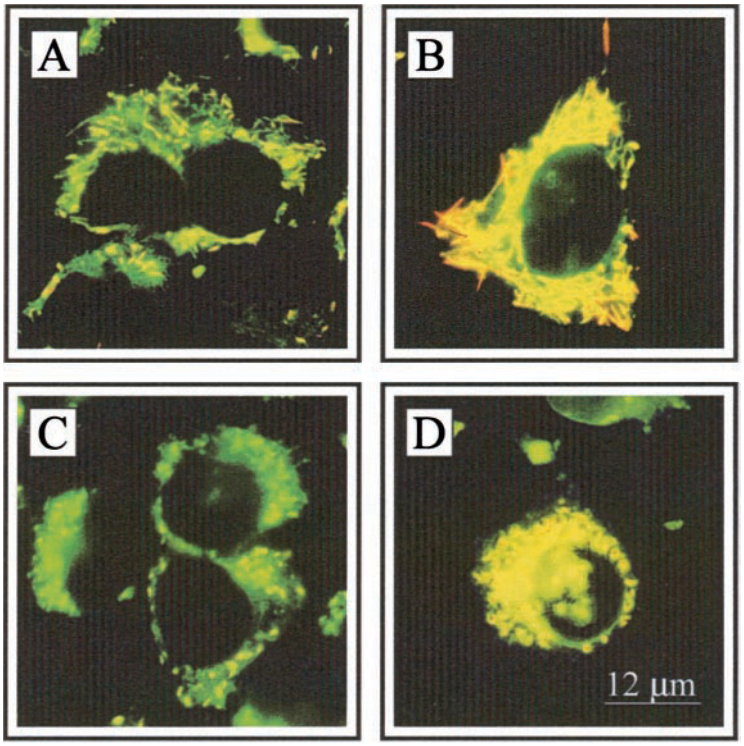

FIGURE 3 Osteosarcoma cells stained with JC-1. Orange regions have a higher mitochondrial membrane potential than green regions. (*A*) Control physiological state; (*B*) Uncoupling of respiration induced by Nigericin (10 μM); (*C*) Inhibition of respiration induced by Antimycin (10 μg/ml); (*D*) Apoptosis induced by Staurosporine (5 μM).

presence of net flows in the cytosol or cytoskeletal activity. This assertion was tested by constructing displacement histograms for all N filament positions as a function of time (see Fig. 10, below) and observing that the resulting time-dependent spatial probability distributions are well described as symmetric distributions with a mean value equal to zero.

The movement of the reticulum results in complicated spatial trajectories and multiexponential k-dependent time-correlation functions. We now examine this behavior systematically through the results of FICS and DVFM experiments. Our microscopic interpretation of these processes is summarized in the Discussion section.

To fully characterize the dynamic state of reticulate mitochondria, we use both FICS and DVFM. Using FICS, the fluctuations of the modulated fluorescence amplitude, $\delta A(t)$, are used to construct time-correlation functions, $G_k(\tau)$, for specific fringe spacings. These correlation functions are simply related to the self-intermediate scattering function, $F_S(k_G, \tau)$, according to Eq. 8. The correlation function is determined by averaging the fluctuations of the square amplitude of the modulated fluorescence signal over t_{max} time origins,

$$G_k(\tau) = \frac{\frac{1}{t_{max}} \sum_{t_0=1}^{t_{max}} \delta A^2(t_0)\delta A^2(t_0+\tau)}{\frac{1}{t_{max}} \sum_{t_0=1}^{t_{max}} [\delta A^2(t_0)]^2}. \quad (12)$$

The decay time of the autocorrelation function is a measure of the time required for a labeled region to move the distance k_G^{-1}. The information contained in $G_k(\tau)$ is a measure of the complexity of the motion. If $G_k(\tau)$ is a multiexponential decay, more than one type of motion is responsible for the fluorescence fluctuations detected at wave number k and time τ. Figure 5 displays plots of $F_S(k, \tau)$ for JC-1-labeled cells under control physiological conditions (Fig. 5 *A*) and after incubation with Nigericin (Fig. 5 *B*). In each case, measurements were performed at three different wave numbers corresponding to the fringe spacings d_G = 0.55, 0.82, and 1.0 μm.

From the autocorrelation functions, we construct the time-dependent effective mean square displacement, $W(\tau)$, by inverting Eq. 8:

$$W_{eff}(\tau) = -\frac{1}{2}\frac{\ln G_k(\tau)}{k_G^2}. \quad (13)$$

TABLE 1 Effects of drugs on metabolic activity

Drug	Concentration (μM)	Incubation Time (min)	Effect
Nigericin	10	30	Respiratory chain uncoupler
Antimycin A	10	10	Respiratory chain inhibitor
Latrunculin A	5	10	De-polymerization of cytoskeletal filaments
Staurosporin	1	240	Initiation of apoptosis

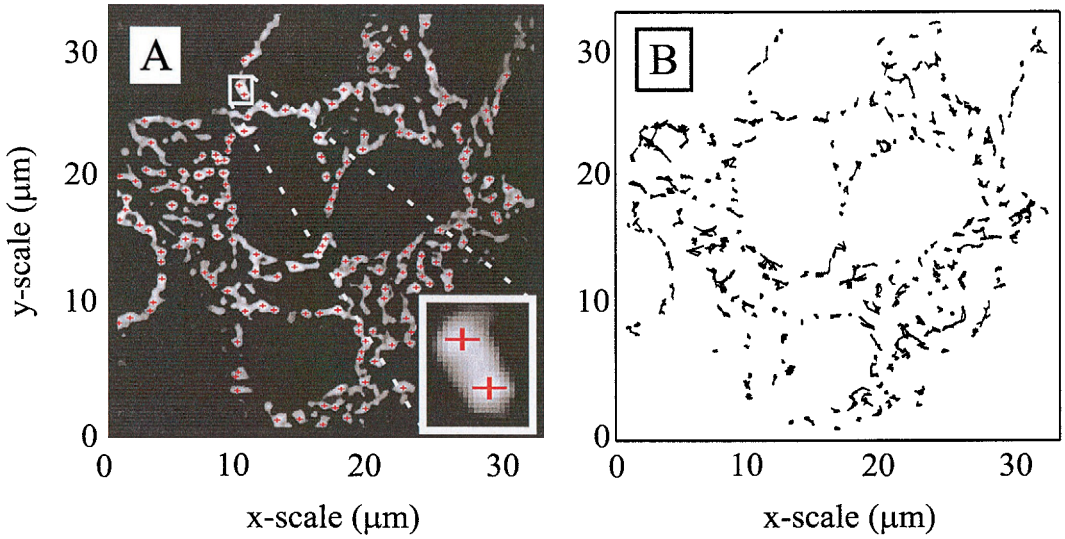

FIGURE 4 (*A*) Digitally processed fluorescence image of osteosarcoma cells labeled with MitoTracker Orange. Filament positions are determined by local pixel brightness and shape (*inset*) according to the prescription given in the text. (*B*) Trajectories of filament positions are computed from 100 sequential frames acquired at 0.172 frame s^{-1}.

In Fig. 6, *A* and *B,* we display plots of $W_{\text{eff}}(\tau)$ corresponding to the data shown in Fig. 5. As noted previously, the mean square displacement is an independent function of k_G for systems undergoing purely diffusive motion. For a purely diffusive system, $W_{\text{eff}}(\tau) = D\tau$, and all measurements made at different fringe spacings yield a single line with slope D. Our measurements of $W_{\text{eff}}(\tau)$ taken at fixed wave number are clearly k-dependent and exhibit time windows with distinctly different slopes. For both control (Fig. 6 *A*) and Nigericin-treated cells (Fig. 6 *B*), the mean square displacement corresponding to $d_G = 0.55$ μm is distinctly smaller at all times than for 0.82 and 1.0 μm. At very short times ($\tau <$ 1 s), local filament regions primarily undergo independent motion with short-time self-diffusion coefficient D_S^S. For intermediate times (1 s $< \tau <$ 20 s) and for short-range displacements ($d_G \leq 0.55$ μm) the local filament regions begin to experience interactions with their surroundings. The effect of these short-range interactions is to modify the self-diffusion coefficient on the time scale that these interactions occur ($\tau_I \sim 15$ s) to a smaller value than D_S^S. Here we define the time scale of this transition in dynamic behavior as τ_I. At these intermediate time and length scales, the time- and k-dependent functional form of $W_{\text{eff}}(\tau)$ is indicative of a kinetic transition from short-time filament motion to a modified long-time diffusion, $\tilde{D}_S^L$, that is effectively "dressed" by collective interactions. Such collective interactions are the mechanism that gives rise to long-range filament displacements, which are probed by large fringe-spacing measurements. In the limit of sufficiently large fringe spacing (short wave number) and time scales long compared to τ_I, the effective diffusion coefficient is no longer a "self" quantity, but rather a reflection of the decay of fluctuations in the collective filament distribution of large spatial extent. In this "hydrodynamic" limit, $\tilde{D}_S(k \to 0, \tau \to \infty) = D_C$ can be identified as the same collective diffusion coefficient as would be measured in

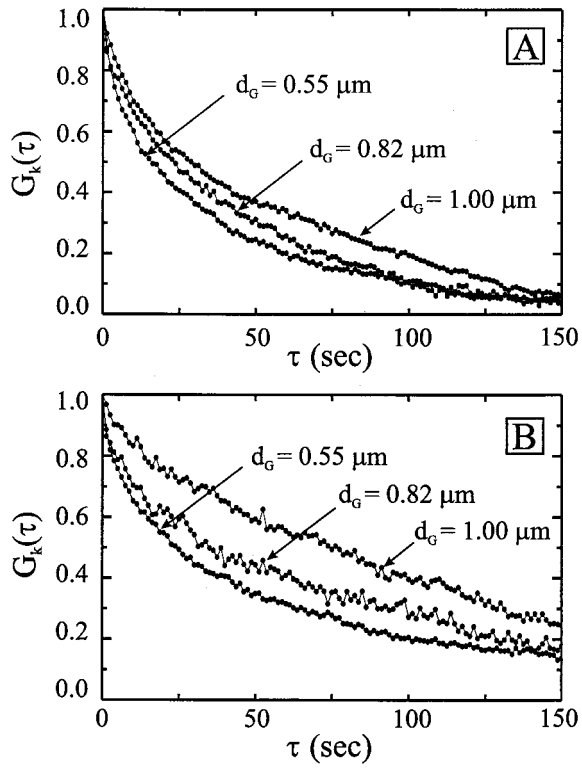

FIGURE 5 Wave number-dependent time-correlation functions, $G_k(\tau)$, obtained from FICS experiments performed on JC-1 labeled cells. Measurements correspond to three different fringe spacings. (*A*) Control physiological conditions; (*B*) After exposure to Nigericin.

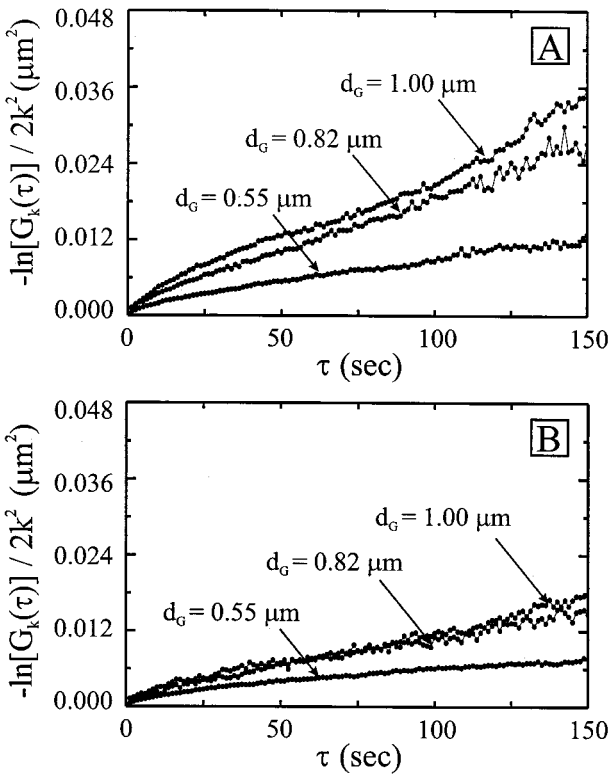

FIGURE 6 Time-dependent effective mean-square displacement, $W_{\text{eff}}(\tau) = -\ln[G_k(\tau)]/2k^2$, constructed from FICS data. (*A*) Control physiological conditions; (*B*) After exposure to Nigericin.

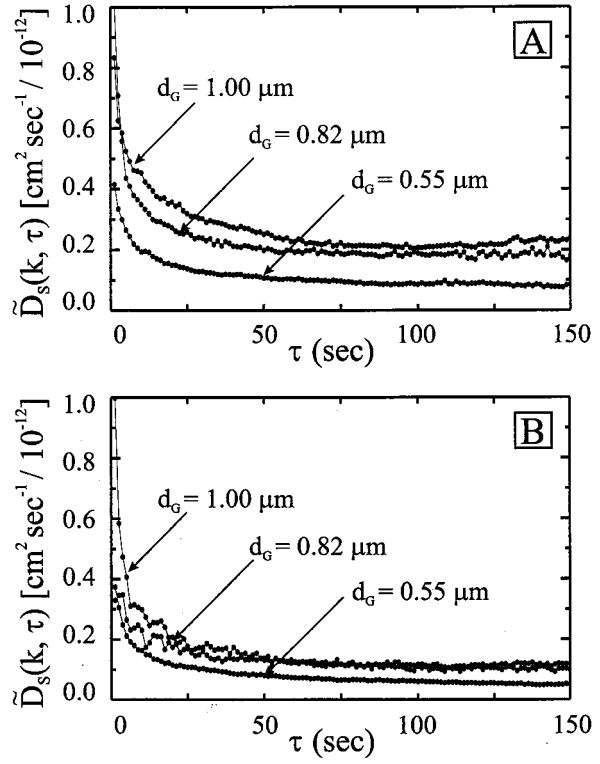

FIGURE 7 Wave number and time-dependent effective diffusion coefficient, $\tilde{D}_S(k, \tau)$, constructed from FICS data according to Eq. 7. (*A*) Control physiological conditions; (*B*) After exposure to Nigericin.

conventional gradient-diffusion measurements (Boon and Yip, 1980).

The kinetic behavior of the mitochondrion can be examined directly from the time- and wave number-dependent effective diffusion coefficient. We calculate $\tilde{D}_S(k, \tau)$ from $W(\tau)$ according to Eq. 7. In Fig. 7, *A* and *B,* we display plots of $\tilde{D}_S(k, \tau)$ corresponding to the data shown in Figs. 5 and 6. For intermediate times (1 s $< \tau <$ 60 s) and fixed k, $\tilde{D}_S(k, \tau)$ decreases continuously, which is consistent with our interpretation that the time-dependence of $W_{\text{eff}}(\tau)$ is the signature of a kinetic transition from local filament short-time motion to a dressed collective long-time diffusion. The values for $\tilde{D}_S(k, \tau)$ lie in the range $3.5–0.5 \times 10^{-12}$ cm^2 s^{-1} and are listed in Tables 2 and 3. We now examine the k-dependence of $\tilde{D}_S(k, \tau)$ at fixed τ. In Fig. 7, *A* and *B,* the effective diffusion coefficient at all times is consistently smaller for large k (or small filament probe volume, $d_G \sim 0.55$ μm) than it is for progressively decreasing k (or incrementally large filament probe volumes, $d_G \sim 0.55$ μm) than it is for progressively decreasing k (or incrementally large filament probe volumes, $d_G \sim 0.82$, 1.0 μm). This behavior is a well-known property of the dynamics of complex fluids where the rates of collective particle fluctuations, as a consequence of local structure, may be greater than the corresponding rates of single-particle motion (Boon and Yip, 1980; Berne and Pecora, 1976). We note that for all k, $\tilde{D}_S(k, \tau)$ reaches its long-time asymptotic value for $\tau >$ 60 s. From the available data, we observe that, for long times and small k, the diffusion coefficient appears to approach a limiting value, $\tilde{D}_C^L$. Our observations suggest that the kinetic transition from short- to long-time dynamic behavior is the result of a structural rearrangement of the local mitochondrial filament environment in the range of length scales 0.55 μm $< d_G <$ 0.82 μm for Nigericin-treated cells (Fig. 7 *B*), and 0.82 μm $< d_G \leq$ 1.0 μm for cells under control physiological conditions (Fig. 7 *A*). We

TABLE 2 Effective diffusion coefficient and power-law exponents from FICS data of JC-1 stained osteosarcoma cells (control physiological conditions)

Time Interval (s)	Fringe Spacing 0.55 μm $\tilde{D}/10^{-12}$ (cm^2 sec^{-1})	m	0.82 μm $\tilde{D}/10^{-12}$ (cm^2 sec^{-1})	m	1.0 μm $\tilde{D}/10^{-12}$ (cm^2 sec^{-1})	m
0–15	1.53	0.62	2.73	0.50	3.50	0.66
15–50	0.84	0.64	1.58	0.67	2.00	0.66
50–100	0.62	0.65	1.69	0.88	1.71	0.76
100–150	0.55	0.66	1.87	1.01	3.06	1.37

Values for $\tilde{D}$ and m are calculated from Eqs. 7 and 15, respectively.

TABLE 3 Effective diffusion coefficient and power-law exponents from FICS data of JC-1 stained and Nigericin-treated osteosarcoma cells (uncoupled respiration)

Time Interval (s)	Fringe Spacing 0.55 μm $\tilde{D}/10^{-12}$ (cm^2 sec^{-1})	m	0.82 μm $\tilde{D}/10^{-12}$ (cm^2 sec^{-1})	m	1.0 μm $\tilde{D}/10^{-12}$ (cm^2 sec^{-1})	m
0–15	1.11	0.56	1.82	0.45	1.86	0.89
15–50	0.58	0.59	1.03	0.57	0.92	0.59
50–100	0.43	0.62	0.72	0.61	1.08	0.88
100–150	0.26	0.48	0.91	0.90	1.36	1.17

Values for $\tilde{D}$ and m are calculated from Eqs. 7 and 15, respectively.

show below that this long-time long-range motion is related to the structural reorganization of cytoskeletal filaments and to the metabolic state of the cell. We further examine the microscopic details of this process in our discussion of the DVFM data below.

To examine the effects of metabolic activity on mitochondrial dynamics, we used FICS to measure $W_{\text{eff}}(\tau)$ (Eq. 13) for JC-1-labeled cells after incubation with drugs known to alter metabolism. Figure 8 displays direct comparisons between measurements of $W_{\text{eff}}(\tau)$ for control cells and for those treated with the drugs listed in Table 1. We note that the slopes of the corresponding curves define the effective diffusion coefficient. The fringe spacing for these measurements was set to 0.82 μm. In Fig. 8 *A,* we examine Nigericin-treated cells. Nigericin is an uncoupler of respiration. Although Nigericin has the effect of hyperpolarizing the mitochondrial membrane (see Fig. 3 *B*), ATP synthesis through the respiratory chain pathway is effectively turned off. There is, however, some ATP production through glycolysis. For short times ($\tau < 15$ s) the data for the Nigericin-treated cells is indistinguishable from the corresponding control-cell measurement. For long times ($\tau > 15$ s), the slope of $W_{\text{eff}}(\tau)$ is a factor of 1.5 smaller for Nigericin in comparison to control cells. We note that the transition time (~15 s) is the same as the interaction time scale, τ_{I}, obtained from our k-dependent study. Hence, uncoupling of respiration causes the collective interactions that lead to long-range filament displacements to be significantly slowed but not eliminated.

In Fig. 8 *B,* we examine the effects of Antimycin A. Antimycin A is an inhibitor of respiration and induces the progressive loss of mitochondrial membrane potential (see Fig. 3 *C*). Similar to Nigericin, for cells treated with Antimycin A, mitochondrial ATP production is completely halted. Measurements begun after 10-min incubation with Antimycin A show almost identical behavior at short and long times to that observed from Nigericin-treated cells. Both Nigericin- and Antimycin-treated cells show a decreased rate of long-range filament motion. This finding is consistent with the hypothesis that the origin of the long-range filament motion is due to the action of ATP-driven cytoskeletal filaments. Because both Nigericin and Antimycin A affect the energetic level of the cell by inhibiting the production of mitochondrial ATP, this observation suggests that cytoskeletal-assisted motion of mitochondria depends on normal respiration.

In general, we find that the short-time ($\tau < \tau_{\text{I}}$) short-range motion of mitochondrial filaments is independent of metabolic activity. Figure 8 *C* shows our results for cells treated with Latrunculin A that depolymerizes actin filaments, a major component of the cytoskeleton. Our findings are similar to those for Antimycin A- and Nigericin-treated cells. For short times, the data corresponding to control and actin-depleted cells are indistinguishable, whereas for $\tau > 50\text{ s} \gg \tau_{\text{I}}$, the long-range motion is completely turned off. Our observation that short-range motion is independent of metabolic state, and the normal activity of cytoskeletal

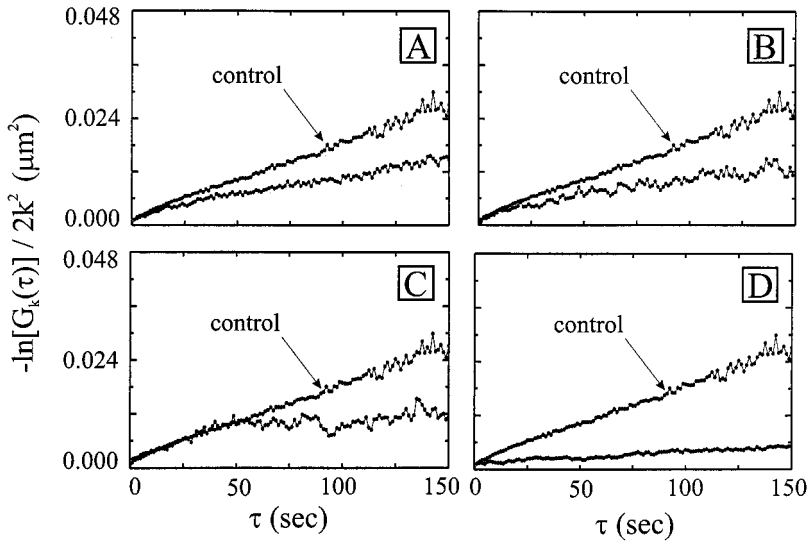

FIGURE 8 The effect of the metabolic state on reticulate mitochondrial motion observed by FICS. The effective mean-square displacement, $W_{\text{eff}}(\tau) = -\ln[G_k(\tau)]/2k^2$, is plotted against τ for fixed wave length $2\pi k_G^{-1} = 0.82$ μm. Each panel represents a comparison between measurements performed in the presence and absence of drug. (*A*) Uncoupling of respiration induced by Nigericin (10 μM); (*B*) Inhibition of respiration induced by Antimycin (10 μg/ml); (*C*) Actin filament depolymerization induced by Latrunculin A (10 μM); (*D*) Apoptosis induced by Staurosporine (5 μM).

filaments suggests that this motion is a consequence of the mechanical properties of the reticulate structure. We expect the short-time motion to exhibit sensitivity to temperature that depends on the elastic properties of the membrane.

Our interpretation of the short-time dynamical behavior of the reticulum having a purely elastic origin is further supported by our measurements using Staurosporine (5 μM), a protein kinase inhibitor that induces apoptosis. As shown in Fig. 3 *D,* this drug dramatically affects mitochondrial structure with the initial swelling and eventual disruption of the membrane. Our comparison between control cells and those treated with Staurosporine are shown in Fig. 8 *D.* In this case, both short- and long-time mitochondrial motions are dramatically reduced. The reduction of the effective mean square displacement at short times is consistent with the expected behavior of a swelled membrane because its surface tension is much larger than that for control cells. The absence of motion at long times is consistent with the fact that oxidative phosphorylation becomes uncoupled early in the programmed cell death process (Mignotte and Vayssiere, 1998). The lack of long-time motion is an indication that cytoskeletal activity is shut down under apoptotic conditions.

As mentioned previously, we performed DVFM measurements so that a microscopic mechanism could be assigned to the rates observed by FICS. For this purpose, it is important to establish that the same processes are probed using the two techniques. Figure 9 displays a direct comparison of $F_S(k, \tau)$ determined from the FICS data of control cells (*solid lines*) and from the DVFM data (*circles*) as a function of τ for three different wave numbers. The FICS data were obtained using Eq. 8, whereas the microscopy data were calculated as described in the Methods section. There is very good agreement between the FICS and DVFM data for all three fringe spacings.

For the DVFM experiments, Osteosarcoma cells (143B) were cultured and stained with either MitoTracker Orange or JC-1. Before and after each measurement, the cell morphology was observed in transmitted light to ensure that experimentally induced cell death had not occurred. In Fig. 10, we display histograms of mitochondrial filament displacements in JC-1 labeled cells constructed from DVFM trajectories. To avoid possible image-processing artifacts such as pixel biasing, we required that consistent and reproducible results were obtained from measurements performed at 100× (Fig. 10 *A*) and 250× (Fig. 10 *B*) magnification. We note that the time-dependent shape of the distributions is independent of magnification. These distributions are formally described as the space–time correlation function $G_S(x, \tau)$, which is the probability that a given filament position suffers a positive or negative displacement projected onto the x-axis during a time interval τ. This is the self part of the van Hove correlation function, defined as

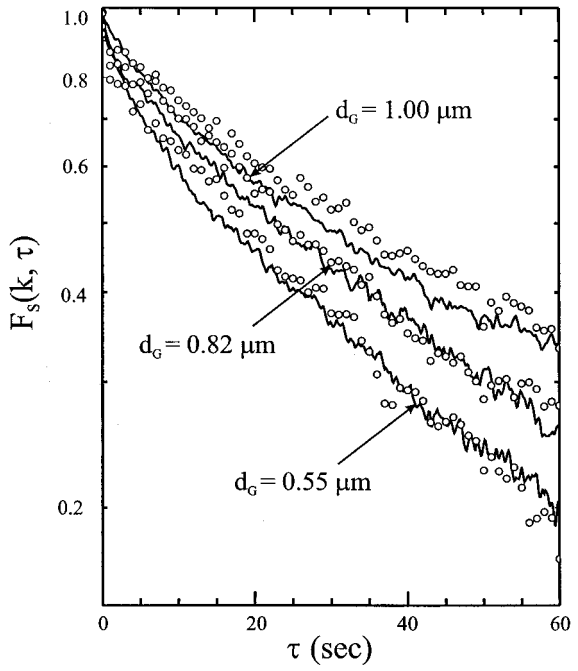

FIGURE 9 Comparison between JC-1 stained mitochondrial filament dynamic structure function, $F_S(k, \tau)$, computed from FICS data (*solid lines*) and from DVFM (*circles*). The latter were obtained by Fourier inversion of DVFM trajectories. The comparison is made for three wave numbers as indicated.

$$G_S(x, \tau) = \frac{1}{N}\left\langle \sum_{i=1}^{N} \delta[x - (x_i(t) - x_i(t + \tau))] \right\rangle. \quad (14)$$

For the case of a system undergoing purely diffusive motion, $G_S(x, \tau)$ is a single-mode Gaussian distribution with a second moment (given by $W(\tau) = \langle [x_1(t) - x_1(t + \tau)]^2 \rangle / 2$) that increases as a linear function of time. The spatial probability distributions shown in Fig. 10 are symmetric and well behaved. Nevertheless, they cannot be described as simple Gaussian distributions. For intermediate times ($\tau \sim \tau_I$), a broad but distinct secondary peak can be seen to develop in $G_S(x, \tau)$ centered at $x = \pm 0.8$ μm. At long times ($\tau \gg \tau_I$), the distribution becomes single mode. We see that the primary peak (centered at $x = 0$) represents randomly oriented short-range displacements, and the secondary peaks are due to the occurrence of long-range cooperative hops. The maximum value of the secondary peaks is most pronounced when $\tau \sim \tau_I = 15$ s. The two types of dynamic processes identified in the distributions $G_S(x, \tau)$ correspond to the short-time thermally activated process and the long-time ATP-driven process observed in our FICS experiments. The interaction time and distance scales measured by FICS ($\tau_I \sim 15$ s, $d_I \sim 0.8$ μm) are in close agreement with the characteristic time and length scales associated with the secondary peak in $G_S(x, \tau)$. Thus, cooperative dynamics are

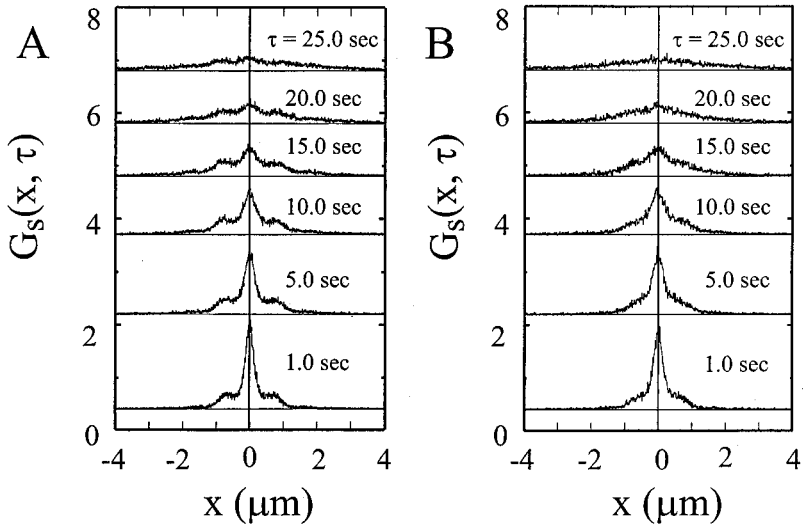

FIGURE 10 The distribution of mitochondrial displacements along the *x*-axis is represented as a function of time (s) and distance (μm). The distributions have been shifted along the vertical axis so that their shapes can be easily examined. We show the evolution in time of mitochondrial displacement histograms in cells stained with JC-1 in experiments performed at (*A*) 100× and (*B*) 250× magnification. Bimodal distributions reveal the presence of two contributions to the dynamics of the reticulum.

the collective interactions that give rise to the observed kinetic transition from short-time local motion to long-time dressed collective diffusion, as discussed above. It is known that the secondary peaks in the distributions $G_S(x, \tau)$ would not be present unless the long-range hops occur in a cooperative fashion (Marcus et al., 1999). That is, within a time period in which a labeled filament position undergoes a long-range displacement, there is a high probability that another nearby filament position will also undergo a long-range displacement. This is consistent with the interpretation that the majority of long-range hopping displacements occur along the contour length of a given mitochondrial filament.

We now examine the time dependence of the mean-square displacement, $W(\tau) = \langle[\mathbf{r}_1(t) - \mathbf{r}_1(t + \tau)]^2\rangle/4$. To characterize the mode of motion being probed, we determine the scaling of $W(\tau)$ with τ according to the equation,

$$W(\tau) = \alpha(k) \cdot \tau^m, \tag{15}$$

where α is a wave number-dependent constant equal to the diffusion coefficient for $m = 1$. The coefficient m has the following significance: if $m = 1$, the motion is diffusive; if $m > 1$, the motion is directed; and if $m < 1$, the motion is spatially constrained (due to confinement or anomalous diffusion; Saxton and Jacobson, 1997). The power-law exponent m represents the slope of the lines obtained by plotting the mean square displacement versus the time interval τ on a log–log scale.

As a control, we investigated the dynamics of dilute suspensions of Rhodamine-labeled 1 μm poly(styrene) spheres in 25% sucrose solution, confined between the glass walls of a narrow capillary cell (wall spacing $\sim$ 1.2 μm). In dilute suspension, the poly(styrene) spheres are expected to undergo quasi-two-dimensional Brownian motion and exhibit Fickian dynamics. The short-time diffusion coefficient can be assigned the same value as the bare diffusion constant, namely, $D_0 = 0.707\ k_BT/6\pi\eta a = 1.3 \times 10^{-9}$ cm^2 s^{-1}, calculated from the Stokes–Einstein equation with the necessary correction to account for the hydrodynamic friction due to the effect of the cell walls (Happel and Brenner, 1963). The diffusion coefficient extracted from our data shown in Fig. 11 *C* ($D = 1.2 \times 10^{-9}$ cm^2 s^{-1}) is in excellent agreement with the theoretical value. Our analysis shows that the dynamics of poly(styrene) spheres is governed by a purely diffusive mechanism ($m = 0.96$), as expected.

Figure 11, *A, B,* and *C,* shows plots of $W(\tau)$ evaluated from our trajectory data. Measurements were performed on cells stained with two different dyes (MitoTracker Orange and JC-1), two magnifications (100× and 250×), and three different frame acquisition speeds (1, 0.172, and 0.048 s^{-1}). In Fig. 11 *A,* we compare measurements of MitoTracker Orange-stained cells performed at 100× (and 0.172 s^{-1}) and 250× (and 1 s^{-1}) magnification. Over the full range of time-scales investigated (1 s $< \tau <$ 120 s), we find that the motion is constrained ($m = 0.7$) for MitoTracker Orange-stained cells. In Fig. 11 *B,* we compare the behavior of MitoTracker Orange with that of JC-1 stained cells, performed at 100× magnification. We repeat this comparison for measurements performed at 250× magnification in Fig. 11 *C.* The results of Fig. 11 are summarized in Table 4.

At short times ($\tau < \tau_I$), JC-1 stained cells exhibit restricted motion ($m = 0.7$), whereas for long times ($\tau > \tau_I$), the motion is in the process of becoming diffusive ($m = 0.88$; *Fig*., *B* and *C*). Similar values for m are obtained from an analysis of the FICS data shown in Fig. 6, *A* and *B,* and are given in Tables 2 and 3. This observation suggests that, in JC-1 labeled cells, "cage effects" dominate the character of the short-time motion where the local environment surrounding a filament position inhibits large displacements. At long times, local rearrangements can only occur through the correlated "hopping" of many filament positions along

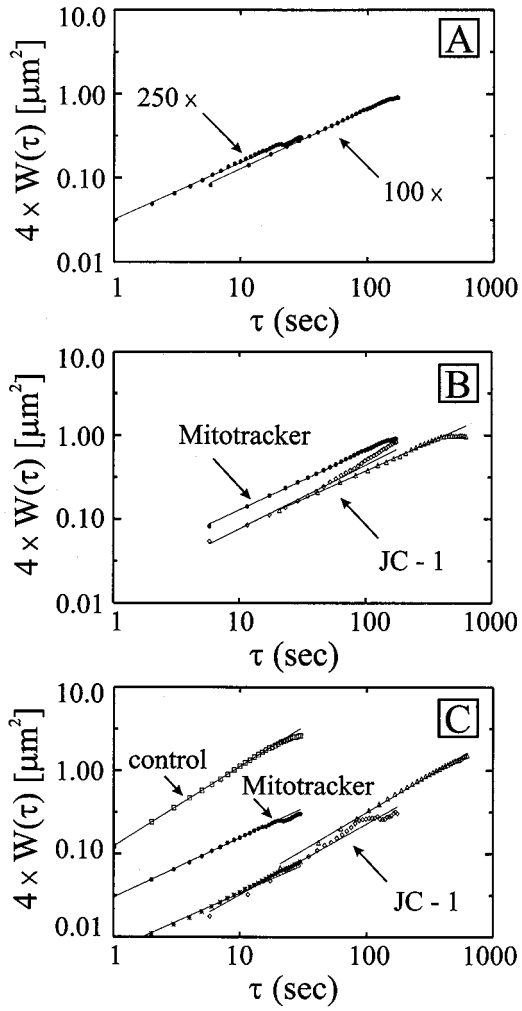

FIGURE 11 Time-dependent mean-square displacement, $W(\tau) = \langle[\mathbf{r}_1(t) - \mathbf{r}_1(t + \tau)]^2\rangle/4$, evaluated from mitochondrial filament trajectories. The slopes of these lines give the power-law exponent, m, that is an indicator of the type of motion ($m < 1$ indicates confined motion, $m = 1$ indicates diffusive motion). (*A*) MitoTracker Orange-stained cells at two magnifications (100× and 250×) and two frame acquisition speeds (1 frame s^{-1} and 0.172 frame s^{-1}). On all time scales examined, motion is confined ($m < 1$). (*B*) Comparison between MitoTracker Orange and JC-1 stained cells at 100× magnification. (*C*) Comparison among MitoTracker Orange, JC-1 stained cells, and control measurements at 250× magnification. Control experiments performed with 1-μm diameter poly(styrene) beads indicates diffusive dynamics ($m \sim 1$). In both (*B*) and (*C*), at short times ($\tau < 15$ s), motion is confined. For $\tau > 60$ s, the motion becomes diffusive ($m \sim 1$).

the contour length of a filament. The time scale of the onset of correlated motion ($\tau \sim \tau_l$) is given by the rate at which the local filament environment (the "cage") can relax its structure through the movement of cytoskeletal filaments. Our observation that MitoTracker Orange-stained cells appears to follow a confined mode of motion over the entire range of investigated time scales can be interpreted in two ways. Either the hopping motion is completely absent in MitoTracker Orange-stained cells, or the hopping motion is observed more effectively when the stain is JC-1. In our JC-1 experiments, the excitation and detection wavelengths are 532 and 570 nm, respectively, so that only the local mitochondrial regions with high membrane potential are observed. A possible interpretation of our data is that regions with high membrane potential have a greater probability to undergo a long-range displacement than do regions with low membrane potential. We discuss this possibility further below.

TABLE 4 Power-law exponents from DVFM data (Fig. 11)

Dye	Short-time ($\tau < 15$ s)	Long-time ($\tau \gg 15$ s)
MitoTracker Orange	0.74	0.72
JC-1	0.75	0.88
Rhodamine poly(styrene) spheres	0.96	—

To distinguish between possible differences in the behavior of cells labeled with MitoTracker Orange and those labeled with JC-1, we performed direct inspections of the microscopic trajectories corresponding to the two systems. In Fig. 12 are plotted trajectory maps of local mitochondrial filament displacements from MitoTracker Orange-labeled cells. Each map consists of 10 sequentially linked filament positions so that the full time duration is 58 s (1 time step = 5.8 s). Arrowheads indicate the direction of the last displacement in the sequence. Inspection of Fig. 12 reveals that the local filament positions are spatially segregated into two subpopulations: those that undergo randomly oriented restricted motion within localized regions of less than 0.1 μm and those that appear to move freely in string-like channels of $\sim$1 μm length. Figure 12, *A* and *B,* is a comparison between the trajectory maps constructed from the first 10 frames (sequence 0–10) and those of the last 10 frames (sequence 10–20) of a 20-frame sequence. The magnified insets illustrate the transient nature of the dynamic heterogeneity. Although the filament positions are always partitioned between mobile and immobile subpopulations, the identities of the filament positions assigned to either group change in time, thereby demonstrating that mobile domains exist in this system as a consequence of collective fluctuations resulting from the activity of cytoskeletal filaments. This observation is consistent with the interpretation that local regions of reticulate mitochondria constantly interconvert between mobile and immobile states. Trajectories computed from similar experiments performed on JC-1 labeled cells (at both 100× and 250× magnification) revealed the same qualitative behavior as that shown in Fig. 12. We conclude that the results obtained are not a pathological effect of the fluorescent probes on mitochondrial dynamics.

Further support for our mechanistic assignments to the modes of mitochondrial motion is provided by examining trajectory maps as a function of image frame-acquisition

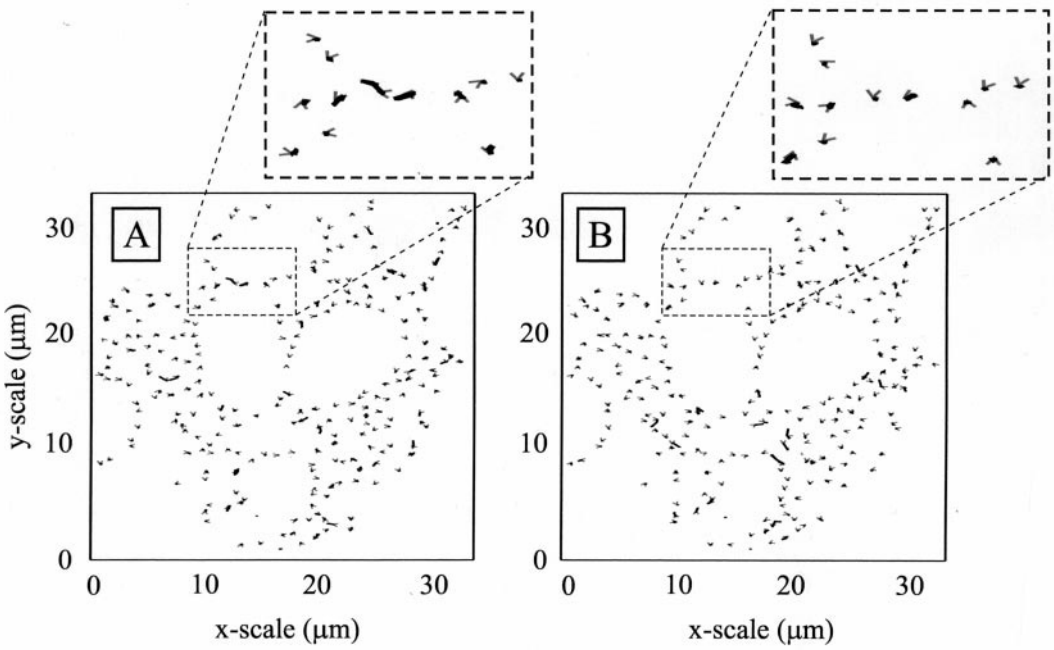

FIGURE 12 Mitochondria trajectories reveal the existence of two dynamic states: short-time short-range motion and long-time long-range motion. Both motions are multidirectional and the dynamic state changes on a time scale of 15 s. Trajectories are shown in black and a gray arrowhead marks the direction of the last displacement. (*A*) Mitochondrial trajectories developed over the first 52 s (frames 0–9); (*B*) Trajectories developed over the subsequent 52 s (frames 10–19). The insets show the transition in the dynamic state of two specific mitochondrial regions.

rates (experimental sampling frequency). This is equivalent to computing trajectories from sequences of images separated by progressively longer time intervals. Figure 13, *A–D* shows trajectory maps constructed from 10 sequential image frames separated by 5.8, 11.6, 23.2, and 46.4 sec, respectively, taken from the same data set. As discussed above, when the filament positions are probed at a frequency of 0.172 s^{-1} (Fig. 13 *A*) the motion is mostly localized so that only a few long-range displacements are detected. The time-dependence of $W(\tau)$ in this time window ($\tau < \tau_I$) is characteristic of constrained motion ($m \cong 0.7$) and the dynamic behavior of the reticulum appears spatially heterogeneous. As the motion is probed at a lower frequency (0.086 s^{-1}, 0.043 s^{-1}; Fig. 13, *B* and *C,* respectively), the long-range hopping motion becomes statistically more prominent, and the spatial distribution of mobile filaments becomes progressively more uniform. In the limit of zero sampling frequency (long-times), we expect the successive occurrence of many long-range hopping events to lead to a completely uniform appearance for the distribution of mobile filaments. For the lowest sampling frequency shown (0.0216 s^{-1}, Fig. 13 *D*) this long-time limit for the MitoTracker Orange-stained system has not yet been achieved. This is consistent with our observation that the character of the motion appears constrained for long times ($\tau \gg \tau_I$) in MitoTracker Orange-stained cells (Fig. 11 *A*). This is not the case for JC-1 stained cells because the observed long-time scaling-law exponent is $m \cong 0.9$ (Fig. 11, *B* and *C*). Thus, for JC-1 stained cells, the observed collective fluctuations approach a diffusive character for $\tau > \tau_I$. In JC-1 and MitoTracker Orange stained cells, both short-range constrained motion and long-range hopping processes are directly observed. Nevertheless, the time scale for which the hopping process becomes dominant is larger for MitoTracker Orange than for JC-1. We conclude that the only possible explanation for the discrepancy between the two measurements is that local regions of the mitochondria with high membrane potential (the only locations of the membrane probed in the JC-1 measurements) are the same regions that undergo cytoskeletal-assisted long-range motion.

DISCUSSION

We have presented a novel implementation of fluorescence-detection methods to fully characterize and assign mechanisms to the rates of motion of the mitochondrial reticulum in live cells. This was accomplished by combining FICS and DVFM. FICS is a newly developed method that is designed to measure, under low signal conditions, the rates of motion in complex fluids as a function of spatial scale. The combination of FICS with DVFM allows the underlying mechanism of the observed rates to be determined. The two methods are mutually complementary. Whereas DVFM reveals the details of microscopic particle trajectories, FICS

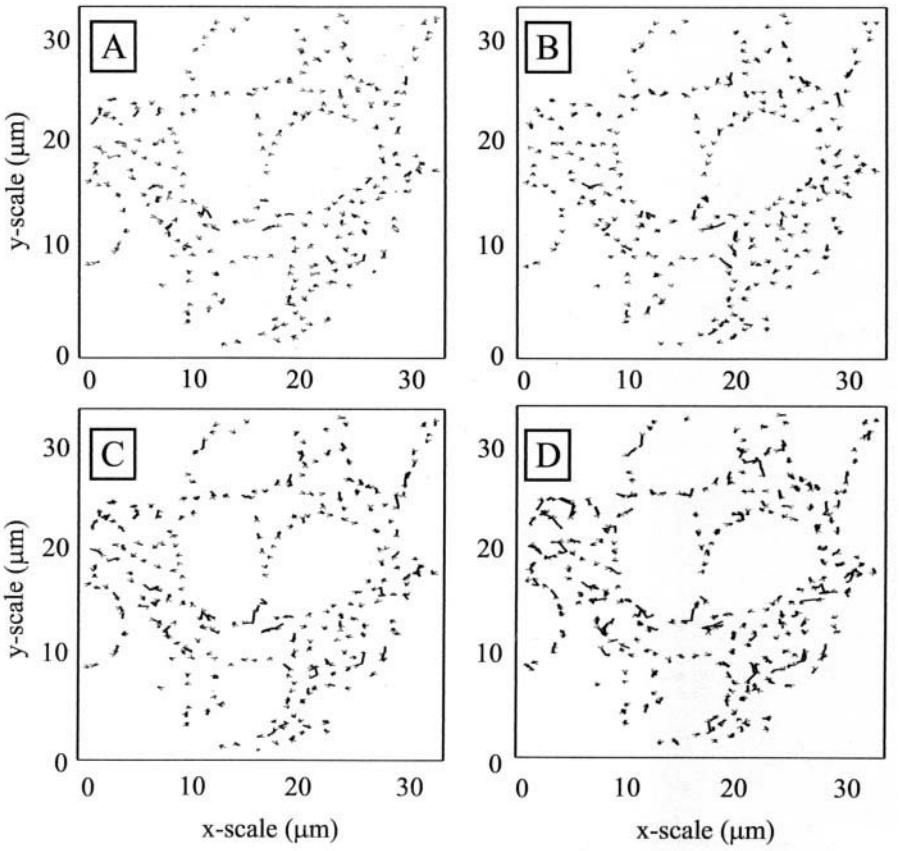

FIGURE 13 Short-time versus long-time motion. Panels (*A*)–(*D*) display mitochondrial trajectories computed from 10 sequential frames separated in time by progressively longer intervals: 1 frame every (*A*) 5.8 s, (*B*) 11.6 s, (*C*) 23.2 s, and (*D*) 46.4 s. The inset from (*A*) shows that, at short time intervals (motion sampled frequently), mitochondria dynamics appears heterogeneous because short-range displacements coexist with long-range displacements. Instead, when motion is sampled less frequently (inset form *D*), the long range displacements are predominant, and, overall, the motion appears homogeneous. Trajectories are shown in black and the direction of the last displacement is marked by a gray arrowhead.

can rapidly acquire large quantities of data to easily determine statistical information.

We have applied this approach to study the dynamics of a structurally complex intracellular organelle: the mitochondrion. The idea that the mitochondrial compartment of the cell can exist as a reticulum has recently attracted increased attention (Bereiter-Hahn and Voth, 1994; Rizzuto et al., 1998a). However, the fundamental properties of this reticulum are poorly understood. In terms of functional significance, it is now clear that the intracellular environment is naturally heterogeneous with spatially varying energetic requirements. A reticulate structure, possibly itself composed of separate interconnected compartments, might be ideally suited to function under heterogeneous conditions. For example, the long thread-like tubes of the reticulum could serve as 'cables' along which the mitochondrial membrane potential (or the ATP gradient) is transported to reach cellular regions with the most urgent energy needs (Bereither-Hahn, 1990; Bereither-Hahn and Voth, 1994; Amchenkova et al., 1988). Alternatively, the network of interconnected tubes could be an important structural support for the strategic location of point contacts with the endoplasmic reticulum where Ca^{2+} uptake occurs as a means of intracellular regulation of metabolic activity (Fall and Bennett, 1999; Rizzuto et al., 1998a; Romashko et al., 1998). As a support structure, the mechanical behavior of this network system should play a critical role in intracellular energy regulation. The recent finding that different respiratory states of mitochondria coexist in a single cell also support the idea that a single mitochondrial reticulum is a heterogeneous structure (Dall'Asta et al., 1997; Nunnari et al., 1997; Reers et al., 1995; Bereiter-Hahn and Voth, 1994). Different values of the mitochondrial membrane potential and different mitochondrial DNA conformations characterize these states.

Our results indicate that the dynamics of the reticulum is composed of two independent contributions, each important on very different time and length scales. On a time scale shorter than $\tau_I \sim 15$ s, the motion of the reticulum is restricted to short distances (<0.8 μm) and is random in direction. This is the expected behavior of local regions of the reticulum confined by a surrounding cage of cytoskeletal filaments. This short time-scale motion is independent of the metabolic state of the cell, suggesting that its origin is due to thermal fluctuations. On a longer time scale ($\tau > \tau_I$), we observe local regions of the reticulum to undergo long-range jump motions directed along the contour lengths of mitochondrial filaments. We assign these infrequent long-range displacements as due to the rate-limiting structural reorganization of the cage formed by the local cytoskeletal network. The frequency of these jumps depends on the physiological state of the cells, however the average

jump distance ($d_I \sim 0.8$ μm) is unaffected by metabolic activity. The occurrence of jumps is completely eliminated by inhibitors of cytoskeletal activity. During short time intervals ($\tau < \tau_I$), discreet regions of the reticulum are spatially segregated into two subpopulations: those that undergo randomly oriented restricted motion, and those that move freely within the restricted space determined by other components of the cell. Although the individual filament regions are always partitioned between mobile and immobile subpopulations, the identities of the filament regions assigned to either group change in time. In the limit of long time intervals ($\tau \gg \tau_I$), the cumulative effect of repeated infrequent jumps leads to the appearance of diffusive motion.

The translocation of the mitochondrion controlled by the cytoskeleton has been observed before in microscopy studies (Tanaka et al., 1998; Bereither-Hahn and Voth, 1994; Rojo et al., 1998; Dittman et al., 1987; Salmeen et al., 1985). An interesting example is the cytoskeletal-assisted motion of mitochondria in neuronal axons and insect ovaria (Dittman et al., 1987), a directed mode of transport (so-called "saltatory" motion) with an average velocity of 50 nm s^{-1}. This value is in excellent agreement with our measurements of the long-time effective diffusion coefficient [$D \sim d^2/4\pi^2\tau = (50\text{ nm})^2/4\pi^2\ (1\text{ s}) = 0.6 \times 10^{-12}$ $cm^2\ s^{-1}$]. In our present studies, for intermediate time scales ($\tau \sim \tau_I$), the cytoskeletal-assisted long-range displacements are biased toward motion along the contour of a mitochondrial filament. In the long-time limit, this directional correlation is lost after a number of long-range jumps have occurred. It is possible that this behavior represents the default dynamic state in cells and serves local energetic requirements until a specific stimulus activates saltatory behavior.

Kinetic transitions and the appearance of dynamic heterogeneity of the kind now observed for mitochondria are an important phenomenon in polymer melts, dense colloid suspensions, and supercooled fluids (Marcus et al., 1999; Guenza, 1999; Cicerone and Ediger, 1996), and are related to their mechanical properties. For a liquid at high densities, the lack of vacancies in the first-neighbor shell surrounding a molecule inhibits large displacements, and local rearrangements can only occur through the collective motion of many particles along pathways that preserve the local continuity of the system. The first-neighbor shell is referred to as a molecular cage. When the time necessary for a molecule to travel a distance equal to the average separation between nearest-neighbor particles is very different from the time scale that the cage structure fluctuates, the system exhibits temporal domains where its dynamics (and mechanical properties) are qualitatively dissimilar. On very short and very long time scales, the system is mobile and behaves like a fluid, whereas on intermediate time scales ($\tau \sim \tau_I$), the system appears immobile and behaves like a solid.

The time scale of the structural relaxation, τ_I, which gives rise to the observed kinetic transition in mitochondria, is controlled by metabolic activity. Thus, alterations in the metabolic state of the cell can enhance or eliminate the kinetic transition and thereby alter the mechanical properties of the reticulum. Further studies, like those reported here, when applied to individual protein components within mitochondria, are needed to understand mitochondrial metabolic processes more fully. The dynamics of the reticulum, as defined here, are the control data for these future studies.

Grants from the National Science Foundation (CHE-9876334 and CHE-9808049), Research Corporation (RI-0138), and the M. J. Murdock Charitable Trust (No. 98181) supported this work. We thank Dr. Mark E. Schmidt for his scientific contributions during the early stages of this project. We also thank Professors Stephen Gregory, Jeff Cina, Robert Mazo, and Marina Gvenza for useful discussions.

REFERENCES

Allen, M. P., and D. J. Tildesley. 1987. Computer Simulations of Liquids, Clarendon Press, Oxford.

Amchenkova, A. A., L. E. Bakeeva, Y. S. Chentsov, V. P. Skulachev, and D. B. Zorov. 1988. Coupling membranes as energy transmitting cables. I. Filamentous mitochondria in fibroblasts and mitochondrial clusters in cardiomyocytes. *J. Cell Biol.* 107:481–495.

Balucani, U., and M. Zoppi. 1994. Dynamics of the Liquid State. S. W. Lovesey, and E. W. J. Mitchell, editors. Clarendon Press, Oxford.

Bereiter-Hahn, J., and M. Voth. 1994. Dynamics of mitochondria in living cells: shape changes, dislocations, fusion, and fission of mitochondria. *Micros. Res. Tech.* 27:198–219.

Bereiter-Hahn, J. 1990. Behavior of mitochondria in the living cell. *Intern. Rev. Cytol.* 122:1–63.

Berne, B. J., and R. Pecora. 1976. Dynamic Light Scattering. Krieger, Malabar.

Boon, J. P., and S. Yip. 1980. Molecular Hydrodynamics. Dover, New York.

Chazotte, B., and C. R. Hackenbrock. 1991. Lateral diffusion of redox components in the mitochondrial inner membrane is unaffected by inner membrane folding and matrix density. *J. Biol. Chem.* 266:5973–5979.

Cicerone, M. T., and M. D. Ediger. 1996. Enhanced translation of probe molecules in supercooled o-terphenyl: signature of spatially heterogeneous dynamics? *J. Chem. Phys.* 104:7210–7218.

Crocker, J., and D. G. Grier. 1996. Methods of digital video microscopy for colloidal studies. *J. Colloid. Interf. Sci.* 179:298–310

Dall'Asta, V., R. Gatti, G. Orlandini, P. A. Rossi, B. M. Rotoli, R. Sala, O. Bussolati, and G. C. Gazzola. 1997. Membrane potential changes visualized in complete growth media through confocal laser scanning microscopy of bis-oxonol-loaded cells. *Exp. Cell Res.* 231:260–268.

Davoust, J., P. F. Devaux, and L. Leger. 1982. Fringe pattern photobleaching, a new method for the measurement of transport coefficients of biological macromolecules. *EMBO J.* 1:1233–1238.

Dittman, F., D. G. Weiss, and A. Munz. 1987. Movement of mitochondria in the ovarian trophic cord of *Dysdercus intermedius* (Heteroptera) resembles nerve axonal transport. *Roux's Arch. Dev. Biol.* 196:407–413.

Fall, C. P., and J. P. Bennett Jr. 1999. Visualization of cyclosporin A and Ca^{2+}-sensitive cyclical mitochondrial depolarizations in cell culture. *Biochim. Biophys. Acta.* 1410:77–84.

Fleming, G. R. 1986. Chemical Applications of Ultrafast Spectroscopy, Oxford, New York.

Gilkerson, R. W., D. H. Margineantu, R. A. Capaldi, and J. M. L. Selker. 2000. Mitochondrial DNA depletion causes morphological changes in

the mitochondrial reticulum of cultured human cells. *FEBS Lett.* 23660: 1–6.

Guenza, M. G. 1999. Many chain correlated dynamics in polymer fluids. *J. Chem. Phys.* 110:7574–7588.

Han, J., and J. Herzfeld. 1993. Macromolecular diffusion in crowded solutions. *Biophys. J.* 65:1155–1161.

Hanson, R. L., X. R. Zhu, and J. M. Harris. 1998. Fluorescence correlation spectroscopy with patterned photoexcitation for measuring solution diffusion coefficients of robust fluorophores. *Anal. Chem.* 70:1281–1287.

Happel, J., and H. Brenner. 1963. Low Reynold's Number Hydrodynamics. Kluwer, Dordrecht, The Netherlands.

Hattori, M., H. Shimizu, and H. Yokoyama. 1996. Fluorescence correlation spectroscopy with traveling interference fringe excitation. *Rev. Sci. Instrum.* 67:4064–4071.

Keitling, U., A. Koltermann, P. Schwille, and M. Eigen. 1998. Real-time enzyme kinetics monitored by dual-color fluorescence cross-correlation spectroscopy. *Proc. Natl. Acad. Sci. USA.* 95:1416–1420.

Knowles, M. K., T. J. Grassman, and A. H. Marcus. 2000. Measurement of the dynamic structure function of fluorescently labeled complex fluids by Fourier imaging correlation spectroscopy. *Phys. Rev. Lett.* (in press).

Luby-Phelps, K. 1994. Physical properties of cytoplasm. *Curr. Opin. Cell Biol.* 6:3–9.

Madden, T. L., and J. Herzfeld. 1993. Crowding-induced organization of cytoskeletal elements. I. Spontaneous demixing of cytosolic proteins and model filaments to form filament bundles. *Biophys. J.* 65:1147–1154.

Marcus, A. H., B. Lin, and S. A. Rice. 1996. Self-diffusion in dilute quasi-two-dimensional hard sphere suspensions: evanescent wave light scattering and video microscopy studies. *Phys. Rev. E.* 53:1765–1776.

Marcus, A. H., J. Schofield, and S. A. Rice. 1999. Experimental observation of non-Gaussian behavior and stringlike cooperative dynamics in concentrated quasi-two-dimensional colloidal liquids. *Phys. Rev. E.* 60: 5725–5739.

Mignotte, B., and J. L. Vayssiere. 1998. Review: Mitochondria and apoptosis. *Eur. J. Biochem.* 252:1–15.

Nunnari, J., W. F. Marshall, A. Straight, A. Murray, J. W. Sedat, and P. Walter. 1997. Mitochondrial transmission during mating in *Saccharomyces cerevisiae* is determined by mitochondrial fusion and fission and the intramitochondrial segregation of mitochondrial DNA. *Mol. Bio. Cell.* 8:1233–1242.

Partikian, A., B. Olveczky, R. Swaminathan, Y. Li, and A. S. Verkman. 1998. Rapid diffusion of green fluorescent protein in the mitochondrial matrix. *J. Cell Bio.* 140:821–829.

Reers, M., S. T. Smiley, C. Mottola-Hartshorn, A. Chen, M. Lin, and L. B. Chen. 1995. Mitochondrial membrane potential monitored by JC-1 dye. *Method. Enzymol.* 260:406–417.

Reers, M., T. W. Smith, and L. B. Chen. 1991. J-aggregate formation of a carbocyanine as a quantitative fluorescent indicator of membrane potential. *Biochem.* 30:4480–4486.

Rizzuto, R., P. Pinton, W. Carrington, F. Fay, K. E. Gogarty, L. M. Lifshitz, R. A. Tuft, and T. Pozzan. 1998. Close contacts with the endoplasmic reticulum as determinants of mitochondrial Ca^{2+} responses. *Science.* 280:1763–1766.

Rizzuto, R., W. Carrington, and R. A. Tuft. 1998b. Digital imaging microscopy of living cells. *Trends Cell Biol.* 8:288–292.

Rojo, G., M. Chamorro, M. L. Salas, E. Vinuela, J. M. Cuezva, and J. Salas. 1998. Migration of mitochondria to viral assembly sites in African swine fever virus-infected cells. *J. Virol.* 72:7583–7588.

Romashko, D. N., E. Marban, B. O'Rourke. 1998. Subcellular metabolic transients and mitochondrial redox waves in heart cells. *Proc. Natl. Acad. Sci. USA.* 95:1618–1623.

Salmeen, I., P. Zacmanidis, G. Jesion, and L. A. Feldkamp. 1985. Motion of mitochondria in cultured cells quantified by analysis of digitized images. *Biophys. J.* 48:681–686.

Salvioli, S., A. Ardizzoni, C. Franceschi, and A. Cossarizza. 1997. JC-1, but not $DiOC_6(3)$ or rhodamine 123, is a reliable fluorescent probe to assess $\Delta\Psi$ changes in intact cells: implications for studies on mitochondrial functionality during apoptosis. *FEBS Lett.* 411:77–82.

Saxton, M. J., and K. Jacobson. 1997. Single-particle tracking: applications to membrane dynamics. *Annu. Rev. Biophys. Struct.* 26:373–399.

Tanaka, Y., Y. Kanai, Y. Okada, S. Nonaka, S. Takeda, A. Harada, and N. Hirokawa. 1998. Targeted disruption of mouse conventional kinesin heavy chain, kif5B, results in abnormal perinuclear clustering of mitochondria, *Cell.* 93:1147–1158.

Thompson, N. L. 1991. Fluorescence correlation spectroscopy. *In Topics in Fluorescence Spectroscopy, Volume 1: Techniques.* J. R. Lakowicz, editors. Plenum Press, New York. 337–378.

Xie, X. S., and J. K. Trautman. 1998. Optical studies of single molecules at room temperature. *Annu. Rev. Phys. Chem.* 49:441–480.